

High Proper Motion Stars in the Vicinity of Sgr A*: Evidence for a Supermassive Black Hole at the Center of Our Galaxy

A. M. Ghez^{1,2}, B. L. Klein, M. Morris, & E. E. Becklin

Dept. of Physics and Astronomy, UCLA, Los Angeles, CA 90095-1562

ABSTRACT

Over a two year period, we have conducted a diffraction-limited imaging study at $2.2 \mu\text{m}$ of the inner $6'' \times 6''$ of the Galaxy's central stellar cluster using the W. M. Keck 10-m telescope. The K band images obtained in 1995 June, 1996 June, and 1997 May have the highest angular resolution obtained at near-infrared wavelengths from ground or space ($\theta_{res} = 0''.05 = 0.002 \text{ pc}$) and reveal a large population of faint stars. We use an unbiased approach for identifying and selecting stars to be included in this proper motion study, which results in a sample of 90 stars with brightness ranging from $K = 9$ to 17 mag and two-dimensional velocities as large as $1,400 \pm 100 \text{ km/sec}$. Compared to earlier work (Eckart et al. 1997; Genzel et al. 1997), the source confusion is reduced by a factor of 9, the number of stars with proper motion measurement in the central 25 arcsec^2 of our galaxy is doubled, and the accuracy of the velocity measurements in the central 1 arcsec^2 is improved by a factor of 4.

The peaks of both the stellar surface density and the velocity dispersion are consistent with the position of the unusual radio source and black hole candidate, Sgr A*, suggesting that Sgr A* is coincident ($\pm 0''.1$) with the dynamical center of the Galaxy. As a function of distance from Sgr A*, the velocity dispersion displays a falloff well fit by Keplerian motion ($\sigma_v \sim r^{-0.5 \pm 0.1}$) about a central dark mass of $2.6(\pm 0.2) \times 10^6 M_\odot$ confined to a volume of at most 10^{-6} pc^3 , consistent with earlier results. Although uncertainties in the measurements mathematically allow for the matter to be distributed over this volume as a cluster, no realistic cluster is physically tenable. Thus, independent of the presence of Sgr A*, the large inferred central density of at least $10^{12} M_\odot / \text{pc}^3$, which exceeds the volume-averaged mass densities found at the center of any other galaxy, leads us to the conclusion that our Galaxy harbors a massive central black hole.

¹Sloan Fellow

²Packard Fellow

Subject headings: stars:imaging:kinematics – Galaxy:center:kinematics and dynamics – infrared:stars

1. Introduction

Extrapolating from the idea that the highly energetic phenomena observed in very active galaxies are powered by massive central black holes, Lynden-Bell & Rees (1971) suggested more than a quarter century ago that much less active galaxies such as our own Milky Way may also harbor massive, though possibly dormant, central black holes. Early on, indirect support for a central black hole arose from the discovery of the unusual radio source Sgr A*; its non-thermal spectrum (e.g., Serabyn et al. 1997, Beckert et al. 1996), compact size (Rogers et al. 1994) and lack of detected motion (Backer 1994) led researchers to associate it with the putative black hole. Definitive proof regarding the existence of a massive central black hole and its association with Sgr A*, however, lies in the assessment of the distribution of mass in the central few parsecs of the Galaxy. If gravity is the dominant force, the motion of the stars in the vicinity of the putative black hole reveals the mass interior to their orbital radius. Thus, objects located closest to the Galactic Center provide the strongest constraints on the black hole hypothesis.

To probe the inner region of the Galaxy, it is crucial to attain the highest resolution possible. However, turbulence in the Earth’s atmosphere distorts astronomical images and typically limits the angular resolution of long-exposures to $\sim 0.5 - 1$ arcsec, an order of magnitude worse than the theoretical limit for large ground-based telescopes. With a distance of 8 kpc to the Galactic center (Reid 1993), traditional long exposure observations are limited to estimating a central mass constrained only to a volume of radius greater than or equal to ~ 0.1 pc (e.g., Lacy et al. 1980, McGinn et al. 1989, Haller et al. 1996; Genzel et al. 1996). In contrast to long exposures, short exposures such as the one shown in Figure 1a, although distorted by the atmosphere, preserve high spatial resolution information which can be used to recover diffraction limited images via a number of different techniques, such as the relatively simple and straight forward method of “Shift-and-Add” (Christou 1991). Eckart & Genzel (1996, 1997) applied this method to data from the ESO 3-m NTT and achieved a resolution of $0''.15$ in the first proper motion study of the central stellar cluster. This technique applied to data obtained from the W. M. Keck 10-meter telescope provides a unique opportunity to study the Galaxy center at an unprecedented resolution of $0''.05$.

Here we report the initial results of our proper motion study of the Galaxy’s central stellar cluster. Within our $6'' \times 6''$ field of view, the motions of 90 stars are tracked over two years. With two-dimensional velocities as high as 1,400 km/sec, these stars imply a central mass of $2.6 \pm 0.2 \times 10^6 M_\odot$ interior to a radius of ~ 0.015 pc, or densities in excess of $10^{12} M_\odot / pc^3$. This volume-averaged mass density exceeds that inferred so far for the center of any other galaxy. The high mass to light ratio and high density lead us to conclude that our Galaxy harbors a massive central black hole.

2. Observations & Data Analysis

We observed the Galaxy’s central cluster with the Keck I facility near-infrared camera (NIRC; Matthews & Soifer 1993) on the nights of 1995 June 10 - 12, 1996 June 26 - 27, and 1997 May 13 (UT). In order to obtain the highest angular resolution with the maximum sensitivity to stars in this region, measurements were made in the photometric K bandpass ($\lambda_o = 2.2 \mu m$ $\Delta\lambda = 0.4 \mu m$) with a magnified plate scale of $0''.0203/\text{pixel}$, providing a $5''.12 \times 5''.12$ field of view (Matthews et al. 1996). Each year, 3,000 - 6,000 images, with an individual exposure time of 0.13 sec, were obtained in sets of 100. These images were primarily centered on the location of Sgr A*, but a few hundred offset frames were also obtained in order to generate a mosaic of a larger region that includes 2 SiO maser sources - IRS 7 and 10ee (Menten et al. 1997) - thereby linking the infrared and radio reference frames, and securing the position of Sgr A* to ± 10 mas (1σ).

Conversion of the raw data into diffraction-limited images proceeds in two steps: (1) calibration of the individual frames and (2) creation of the shift-and-add maps. First, the standard image analysis steps of sky subtraction, flat fielding, and bad pixel correction remove the majority of the measurement artifacts from the individual frames, which are known as specklegrams. A few additional operations occur at this initial stage of analysis; a small area ($\sim 12\%$ of the field of view), which is contaminated by the unmagnified field (cf. Matthews et al. 1996), is masked off, the camera’s distortion is accounted for (see Appendix for details), each pixel is expanded into 2×2 pixels with equal flux, in order to prevent degradation of the image quality when shifting the specklegrams by fractions of a pixel, and, finally, the specklegrams are rotated through the parallactic angle specified in the header such that they have a common orientation³. After this first stage of data

³In these experiments, the image rotator was turned off such that the field orientation on the detector changed throughout the night. This procedure minimizes the systematic effects of possible flat fielding imperfections and image distortion, and maximizes the sky coverage in the final shift-and-add maps.

processing the specklegrams are free of camera artifacts and are dominated by the short exposure structure of the 4 brightest stars, IRS 16 NE, IRS 16 NW, IRS 16 C, and IRS 16 SW ($K \sim 9\text{-}10$ mag; see Figure 1a).

In the second stage of data reduction, the frames are combined to form shift-and-add maps. Each star in the individual exposures is distorted by the atmosphere in the same way, indicating that the field of view is well within the near infrared isoplanatic patch, and has a pattern that is dominated by one bright diffraction-limited spot (or speckle). By adding together the specklegrams, shifted to align the brightest speckle of a reference source (IRS 16 C), we generate a shift-and-add image with a point spread function composed of a diffraction-limited core containing $\sim 10\%$ of the light on top of a broad seeing halo (see Figures 1 & 2). Airy rings around the cores of bright stars indicate that the diffraction limit has been truly achieved. The atmospheric conditions during each run are evaluated on the basis of the halo FWHM, which is $0''.5$ in 1995, $0''.8$ in 1996, and $0''.4$ in 1997. Due to field rotation and differences in the centering of individual frames, the field of views of the final shift-and-add images are larger than the original frames, with a $6'' \times 6''$ region containing all the stars reported here.

3. Results

3.1. Stellar Census

The raw shift-and-add maps reveal a large population of faint stars against the seeing halos of the bright IRS 16 stars. The primary objective in the design of the analysis presented here is to generate an *unbiased* sample, which is defined independently of the position of Sgr A*. Stars are identified in each image by applying a “match filter,” generated by cross-correlating the raw shift-and-add image with the diffraction-limited core (out to $r = 0''.06$) of IRS 16 NE, the brightest isolated point source in the field. The values in the correlation map range from 1 for perfectly correlated regions to -1 for perfectly anti-correlated regions; strong peaks, such as the ones shown in Figure 1d, mark the locations of stars. Each peak in the correlation maps exceeding 0.2 is flagged as a *potential* star, and the star’s brightness is estimated by aperture photometry at that location in the shift-and-add map (for details see footnote to Table 1). *Definite* detections are marked for cases which have both a correlation peak exceeding 0.7 and more than 1,000 frames contributing to that location in the final shift-and-add map. Roughly 80 definite detections are made in each map. The final population of stars in each year’s map that is considered in this proper motion study is composed of the set of definite detections for a given year and the matches to the definite detections from the other two years, which are searched

for among the possible detections within a $0''.07$ radius. If more than one match is found, the closest star must be the most similar in brightness or the star is eliminated from the sample due to source confusion. Table 1 lists the 90 stars that are thus identified in all three measurements and comprise the proper motion sample; half of these stars are definite detections in all three years, whereas the other half have definite detections in only one or two years. The latter group arises from (1) the poorer quality of the 1996 map, which causes some stars’ correlation values to drop below the definite detection threshold that year, but nonetheless satisfy the potential star criteria and are matched to definite detections in the other years, and (2) differences in map centers, which results in some stars near the peripheries having more than 1000 contributing frames in at least one map but not in all three. The stars in this proper motion sample have brightness ranging from $K = 9$ to 17 mag, or equivalently $M_K = -8.5$ to -0.5 mag assuming $A_K = 3$ mag, with typical relative positional uncertainties of $\sim 0''.002$ for sources brighter than 15 mag. The naming convention we have adopted is described in Table 1. ⁴

The distribution of stars in the proper motion sample shows a clear central concentration within $0''.2 \pm 0''.1$ of the position of Sgr A* (Menten et al, 1997). It should be noted, however, that our sample of 90 stars itself is neither complete nor uniform. Many stars in the image are missed using the fairly conservative approach and selection criteria described above, which tends to omit close doubles as their correlation values are significantly lower than isolated stars - the smallest separation between two stars in the final sample is $0''.08$. Furthermore, the seeing halos cause the sensitivity to faint sources to grow with distance from bright sources out to $1''.5$ where it is then more or less constant at a brightness ~ 7 mag fainter than the bright source. Nonetheless, with a peak value of $\sim 15 \text{ stars}/\text{arcsec}^2$, the stellar surface density for the proper motion sample appears to manifest a distinct cluster, the Sgr A* (IR) cluster, of stars fainter than $K = 14$ mag and an apparent core radius of $0''.3$ (0.01 pc).

3.2. Stellar Kinematics

Since measuring the motions of stars requires a common coordinate system, the coordinate systems for the three measurements are aligned by minimizing the net displacements of *all* the stars in the proper motion sample, allowing for translation and rotation between the three epochs. Figure 3 shows the transformed positions for stars

⁴The positional uncertainties are based on the variance of the stars’ locations in three independent and equivalent seeing submaps from each year.

within a 1 arcsec^2 region centered on the nominal position of Sgr A*, where motion for several of the stars can be easily seen. Formal two-dimensional velocities are derived by fitting lines to the positions as a function of time, weighted by the positional uncertainties, for all stars in the sample, of which 30 have significant motion ($v/\sigma_v > 4$) over the two year baseline of this study (see Table 1). In all cases, the velocity vectors measured between 1995-1996 and 1996-1997 agree to within 4σ . As a consequence of our approach to defining the proper motion sample the uncertainties are *independent* of the overall location and depend primarily on the source brightness, with typical uncertainties of 50 km/sec for the brighter stars ($K < 13 \text{ mag}$), 100 km/sec for the intermediate brightness stars ($13 \text{ mag} < K < 15 \text{ mag}$), and 200 km/sec for the faintest stars ($15 \text{ mag} < K < 17 \text{ mag}$). Eleven stars have proper motions exceeding 500 km/sec, with the largest velocity reaching $1,400 \pm 100 \text{ km/sec}$, 0.5% the speed of light, for a $K = 15 \text{ mag}$ source $0''.1$ west of Sgr A*.

The distribution of velocities is nonuniform, with the highest velocity sources clustered toward the field center (see Figure 4). Seven of the 11 sources with velocities exceeding 500 km/sec appear to be members of the central Sgr A* stellar cluster, with projected distances from the nominal position of Sgr A* of less than $0''.8$. A map of the two-dimensional velocity dispersion, obtained by binning the velocities over $1''.5 \times 1''.5$ regions, shows a prominent peak of 670 km/sec located just $0''.1$ East and $0''.1$ North of Sgr A*. The coincidence between the nominal position of Sgr A*, the peak of the stellar surface density, and the peak of the velocity dispersion, suggests that Sgr A* is indeed at the dynamical center of our galaxy. We therefore take the position of Sgr A* as the center for the analysis that follows.

With more than one dimension of the velocity vectors measured, we can test for isotropy, in which case the velocity dispersions should be identical in all three dimensions. In the plane of the sky, the projected radially directed (σ_{\parallel}) and the projected tangential (σ_{\perp}) components of the velocity dispersion are similar at all radii covered by this study, with $\sigma_{\parallel}/\sigma_{\perp} = 1.15 \pm 0.1$. Line of sight velocity measurements for individual stars have only been obtained for the largest radii covered here, $\sim 0.1 \text{ pc}$; nonetheless, the velocity dispersion in the line of sight (σ_z) and that of either dimension in the plane of the sky is in agreement, with $\sigma_z / \langle \sigma_{\parallel}, \sigma_{\perp} \rangle = 1.1 \pm 0.2$, as was shown by Genzel et al. (1996). The apparent isotropy of the stellar velocity field suggests that the stars are moving under the influence of a spherical potential.

The apparent isotropy justifies averaging the two components of dispersion in the plane of the sky to examine only a one-dimensional velocity dispersion as a function of projected radius (Figure 5). The velocity dispersion at small radii is clearly much higher than the 50 km/sec dispersion observed at larger radii. Furthermore, fitting these data to a power law, $\sigma_v(r) \sim r^{\alpha}$, results in best fit α of -0.53 ± 0.1 , an excellent match with that expected from

Keplerian orbits ($\alpha = -0.5$). This behavior suggests that *the stars' motions are dominated by the gravitational force of a large central mass confined to a radius less than the smallest radial bin - 0.015 pc*. It also suggests that this central mass completely dominates the mass distribution out to at least the radius of the outermost bin, 0.1 pc.

3.3. Comparison with Other Proper Motion Measurements

Of the 90 stars presented here, roughly half - 44 stars - have velocities also reported by Eckart and Genzel (EG; Eckart & Genzel 1996,1997; Genzel et al. 1997) that differ by no more than 4σ from those in Table 1; the largest differences arise in the central $\sim 1\text{arcsec}^2$ where the source confusion is the largest and the increase in angular resolution has the most impact. Over the $\sim 30\text{arcsec}^2$ area covered by both EG and this study, only 3 of EG's 47 stars are not included in our proper motion sample. One of these - S5 - is resolved as a close, equal-brightness double, causing it to fail our selection criteria, although it is clearly seen in the shift-and-add images. The other two - W15 and S3 - are selected in at least one of our epochs but not all in three. The former is very close to the edge of the field of view and small shifts in the field center cause it to fall below our detection limit in 1996 and 1997, and the latter is coincident with the Sgr A* star cluster where the source confusion is greatest. S3 is identified as a definite detection in 1995, but is dropped from the proper motion sample due to ambiguity when the search for possible matches in the 1996 and 1997 maps reveal several possible solutions that do not satisfy the condition that the closest source has the most similar brightness. Although one of these solutions does produce constant velocity ($880 \pm 200\text{ km/sec}$ at $\text{PA} = 320^\circ$), it and all the other solutions with a search radius of $0''.07$ require the source to fade by 1.5 mag between 1995 and 1996. More frequent observations at as high a spatial resolution as possible are clearly needed to unambiguously track both the motion and variability of sources in this high density region. The proper motions for the remaining 46 stars listed in Table 1, which have magnitudes ranging from 12 to 17, are the first reported values for these stars; they *double* the number of stars with proper motion measurements in this region.

In addition to the proper motion stars, Genzel et al. (1997) also report S12 as a variable star and as a possible infrared-counterpart to Sgr A*. This source is detected as a possible source in our 1996 and 1997 data sets, but does not meet the proper motion selection criteria. The proper motion derived from the 1996 and 1997 measurements, however, is inconsistent with the proper motion limits derived for Sgr A* at radio wavelengths (Backer 1994).

4. The Central Dark Mass

The two-dimensional positions and velocities measured for stars in the inner $6'' \times 6''$ ($0.23 \text{ pc} \times 0.23 \text{ pc}$) provide excellent constraints on the distribution of matter at the center of the Galaxy. In principle, if all six components of the position and velocity vectors could be observed, each star would yield an estimate of the mass enclosed within its radius. With the two-dimensional projections, the individual stars provide only lower limits on the enclosed mass, M_{min} , under the assumption that the stars are gravitationally bound, in which case

$$M_{min} = \frac{v^2 R}{2G}.$$

Every star imposes a minimum mass that exceeds the enclosed mass of luminous matter extrapolated from the power law relationship derived at larger radii by Genzel et al. (1996). Considering only stars with $v/\sigma_v \geq 4$, the minimum enclosed mass estimates reach values of $2 - 3 \times 10^6 M_\odot$, with the apparent members of the Sgr A* cluster having M_{min} 's ranging from $0.2 - 1 \times 10^6 M_\odot$ (see Figure 6). Thus the stars appear to be moving under the influence of a gravitational potential generated by at least a few million solar masses of dark matter.

Projected mass estimators analyze stars grouped in concentric annuli around the dynamical center to account for projection effects and produce estimates of the true enclosed mass. The well-known and frequently used virial mass estimator, M_{virial} , has the form

$$M_{virial} = \frac{3\pi}{2G} \langle v^2 \rangle / \langle 1/R \rangle .$$

Applied to the Galactic center data set, this mass estimator suggests that $2.5 \pm 0.2 \times 10^6 M_\odot$ of dark matter is located predominantly, if not exclusively, at radii smaller than 0.015 pc . Bahcall & Tremaine (1981), however, pointed out that the virial mass is a biased, inefficient, and, in some cases, inconsistent mass estimator; they proposed a set of new projected mass estimators for a tracer population moving under the influence of a central potential, M_{BT} . For the case of isotropic orbits this estimator is given by

$$M_{BT} = \frac{16}{\pi G} \langle v^2 R \rangle .$$

The assumption of a dominating compact central mass is well justified, given the Keplerian fall-off of the velocity dispersion as a function of radius (Figure 5). The validity of this assumption allows one to use the projected mass estimator with only minor caveats about the finite sampling volume (Haller & Melia 1996), implying a possible correction on the order of 10% (which we do not apply).

For the Galactic center data set the two methods produce very similar results, with the M_{BT} values being only slightly larger, $2.6 \pm 0.2 \times 10^6 M_\odot$. These values agree very well with those obtained over similar radial distances by Genzel et al. (1997) and match well with those obtained at larger radii (see Figure 7). Overall, the enclosed mass results suggest, consistent with both the functional form of the velocity dispersion vs. radius and the minimum mass estimates, that the majority of stars observed are moving in a potential dominated by $2.6 \times 10^6 M_\odot$ of matter contained within 0.015 pc of Sgr A*. Since the total luminosity within 0.015 pc of Sgr A* observed in our maps is a meager L_K of $40 L_\odot$, the implied mass to light ratio is $M/L_K \sim 6 \times 10^5$. As the K-band covers only a small range of wavelengths, it is useful to compare this value to that observed for the Sun, which has a M/L_K of ~ 40 . Given the high mass to light ratio observed, the central mass concentration is certainly composed primarily of dark matter.

Strong constraints on the distribution of central dark matter arise from the enclosed mass measurements. Confining the density distribution of dark matter to radii smaller than 0.015 pc implies a minimum density of $10^{12} M_\odot pc^{-3}$, surpassing the volume averaged mass densities inferred for dark matter at the center of any other galaxy by at least two orders of magnitude. One intriguing possibility is that the dark compact object we are observing is a single supermassive black hole, as has been inferred for several other galaxies such as M87 (Ford et al. 1994; Harms et al. 1994) and NGC 4258 (Greenhill et al. 1995; Myoshi et al. 1995). This would be a unique solution if the minimum radius of the enclosed mass measurements corresponded to the Schwarzschild radius for a $2.6 \times 10^6 M_\odot$ black hole ($R_{sh} = 2GM_{bh}/c^2$, $R_{sh,2.6 \times 10^6 M_\odot} = 2.5 \times 10^{-7} pc = 11 R_\odot$), in which case the central “density” would be $\rho_{o,bh} = 4 \times 10^{25} M_\odot pc^{-3}$; however the minimum radius is still a factor of 40,000 larger than R_{sh} and thus other scenarios still need to be explored.

One alternative to the single black hole scenario is a cluster of dark matter in the form of stellar remnants, brown dwarfs, or even elementary particles. In general, astrophysical clusters can often be approximated by a Plummer model, $\rho(r) = \rho_o \left(1 + \frac{r^2}{r_c^2}\right)^{-\alpha/2}$, which requires the specification of two parameters in addition to the central density: a characteristic size scale, r_c , and the power law, α . Although an α of 2 holds for the visible stellar cluster with $\rho_o = 4 \times 10^6 M_\odot/pc^3$ and $r_c = 0.2$ pc, such a profile produces an enclosed mass which increases linearly with radius, much steeper than that observed within the central 0.2 pc. To match the observed flat enclosed mass as a function of radius with a pure cluster model requires α to be at least 3 and r_c to be very small. Since astrophysical systems have been observed with α 's as large as 5, we explored the viability of clusters with α ranging from 3 to 5. Mathematically, dark cluster models can be made to fit the observed data; α of 5 requires a r_c of 0.01 pc and ρ_o of $6 \times 10^{11} M_\odot/pc^3$, α of 4 is fit by r_c of 0.005 pc and ρ_o of $2 \times 10^{12} M_\odot/pc^3$, and α of 3 demands r_c of 0.00002 pc and ρ_o of

$7 \times 10^{18} M_{\odot}/pc^3$ (see Figure 7). Physically, however, such dark cluster models are highly improbable (cf. Maoz 1995, 1998). A viable cluster must have both evaporation and collision timescales greater than the lifetime of the Galaxy ~ 10 Gyr. Clusters of objects having any single mass greater than $0.02 M_{\odot}$ have evaporation timescales shorter than the age of the Galaxy, ruling them out from consideration. Among possible nonluminous cluster members with masses less than $0.02 M_{\odot}$, brown dwarfs, and very low mass objects with cosmic composition are ruled out by their short collisional timescales, which are at most 10^7 years. What has not been eliminated with timescale considerations alone are clusters of elementary particles and very low mass ($M < 0.02 M_{\odot}$) black holes, however such clusters are theoretically unmotivated. Thus, the observed mass distribution is not likely to be due to a pure cluster of dark objects.

Another alternative is for only a fraction of the mass to be in a central black hole with the remaining mass contained in a cluster of dark objects as might be found in a post core-collapsed cluster. Fitting the measured enclosed mass as a function of radius with a black hole plus an $\alpha \sim 2$ cluster model, we find that only 1% of the total mass interior to 0.015 pc can be in the cluster due to rapid rise of the mass enclosed by an $\alpha \sim 2$ cluster. Although larger α clusters relax this criterion, $\alpha \sim 2$ is the expected form for a cluster surrounding a black hole (e.g., Binney & Tremaine 1987). Thus the dynamical evidence, independent of the presence of Sgr A*, leads us to the conclusion that our Galaxy harbors a $2.6 \times 10^6 M_{\odot}$ black hole.

Our Galaxy was neither the first nor an obvious candidate for a central supermassive black hole; however in the million solar mass range, it, along with NGC 4258, has become one of the strongest cases for a black hole. The significance of a central black hole in our normal inactive Galaxy is the implication that massive black holes might be found at the centers of almost all galaxies.

We thank the staff of the W. M. Keck Observatories, especially Joel Aycock, Teresa Chelminiak, Al Conrad, Bob Goodrich, Wendy Harrison, Check Sorenson, and Wayne Wack. Support for this work was provided by NSF, the Packard Foundation, and the Sloan Foundation. The authors are grateful to M. Jura, R. White, and J. Patience for helpful comments. AMG is grateful for the support for this project received from the National Science Foundation Young Investigator Program, the Packard Foundation, and the Sloan Foundation. The data presented herein were obtained at the W. M. Keck Observatory, which is operated as a scientific partnership among the University of California, the California Institute of Technology, and the National Aeronautics Space Administration. The Observatory was made possible by the generous financial support of the W. M. Keck Foundation.

A. NIRC Off-Axis Distortion

NIRC, which sits $\sim 50''$ away from the telescope's optical axis, has a known off-axis distortion which is corrected for by applying the following relations from Gleckler (1995) for the distorted ray positions (x_D, y_D) relative to the true ray positions (x, y) : $x_D = x + Bx + Cxy + Exr^2$ and $y_D = y + A + 3By + Cy^2 + (D + Ey)r^2$ where $r^2 = x^2 + y^2$, $A = -0.00001708$, $B = -0.0002197$, $C = -0.003553$, $D = 0.001778$, and $E = 0.00006560$. The corrected intensity value at each (x, y) is found by bilinear interpolation of the original image at the corresponding distorted ray position, (x_D, y_D) . This procedure reduces the pixel scale variations from 2% to less than 0.5% over the field of view for a single frame. In the final shift-and-add maps, averages over different camera orientations further minimize any residual distortions.

REFERENCES

- Backer, D.C. 1994, in IAU Symp. No. 169: Unsolved Problems in the Milky Way
- Bahcall, J. N., and Tremaine, S. 1981, ApJ, 244, 805
- Bahcall, J. N., and Tremaine, S. 1987, Galactic Dynamics (Princeton: Princeton Univ. Press)
- Beckert, T., Cuschl, W. J., Mezger, P. G., & Zylka, R. 1996, *Å*, 307, 450
- Christou, J. C. 1991, PASP, 103, 1040
- Eckart, A. & Genzel, R. 1996, Nature, 383, 415
- Eckart, A. & Genzel, R. 1997, MNRAS, 284, 576
- Ford, H. C., Harms, R. J., Tsvetanov, Z. I., Hartig, G. F., Dressel, L. L., Kriss, G. A., Bohlin, R. C., Davidsen, A. F., Margon, B., Kochhar, A. K. 1994, ApJ, 435, L27
- Genzel, R., Eckart, A., Ott, T. and Eisenhauer, F. 1997, MNRAS, 291, 219
- Genzel, R., Thatte, M., Krabbe, Kroker, H., & Tacconi-Garman, L. E. 1996, ApJ, 472, 153
- Greenhill, L. J., Jiang, D. R., Moran, J. M., Reid, M. J., Lo, K. Y., Claussen, M. J. 1995, ApJ, 440, 619
- Guesten, R., Genzel, R., Wright, M. C. H., Jaffe, D. T., Stutski, J., and Harris, A. I. 1987, ApJ, 318, 124
- Haller, J. W., & Melia, F. 1996, ApJ, 464, 774
- Haller, J. W., Rieke, M. J., Rieke, G. H., Tamblyn, P., Close, L., & Melia, F. 1996, ApJ, 456, 194
- Harms, R. J., Ford, H. C., Tsvetanov, Z. I., Hartig, G. F., Dressel, L. L., Kriss, G. A., Bohlin, R., Davidsen, A. F., Margon, B., Kochhar, A. K. 1994, ApJ, 435, L35
- Klein, B. L., Ghez, A. M., Morris, M., and Becklin, E. E. 1996, in the proceedings of the PASP Vol. 102
- Lacy, J. H., Townes, C. H., Geballe, T. R., & Hollenbach, D. J., 1980, ApJ, 241, 132
- Lynden-Bell, D. & Rees, M. J. 1971, MNRAS, 152, 461
- Maoz, E. 1995, ApJ, 447, L91
- Maoz, E. 1998, ApJ, 494, L181
- Matthews, K., Ghez, A. M., Weinberger, A. J., and Neugebauer, G. 1996, PASP, 108, 615
- Matthews, K. and Soifer, B. T. 1994, Astronomy with Infrared Arrays: The Next Generation, ed. I. McLean, Kluwer Academic Publications (Astrophysics and Space Science, v. 190, p. 239)

- McGinn, M. T., Sellgren, K., Becklin, E. E., & Hall, D. N. B., 1989, *ApJ*, 338, 824
- Menten, K. M., Reid, M. J., Eckart, A., & Genzel, R. 1997, *ApJ*, 475, L111
- Myoshi, M., Moran, J. M., Hernstein, J., Greenhill, L., Nakai, N., Diamond, P., & Inoue, M. 1995, *Nature* 373, 127
- Reid, M. *ARA&A*, 31, 345
- Rogers, A. E. E., Doeleman, S., Wright, M. C. H., Bower, G. C., Backer, D. C., Padin, S., Philips, J. A., Emerson, D. T., Greenhill, L., Moran, J. M., & Kellermann, K. I. 1994, *ApJ*, 434, L59
- Serabyn, E, Carlstrom, J., Lay, O., Lis, D. C., Hunter, T. R., & Lacy, J. H. 1997, *ApJ*, 490, L77

Fig. 1.— (a) One of the many short exposures ($t_{exp} = 0.13$ sec) obtained on the central stellar cluster. Each star has the same speckle pattern, which is dominated by one bright speckle. (b) By registering all the individual frames with respect to IRS 16 C, a shift-and-add image, such as the one shown for 1995, is constructed. This image has 8 mag of dynamic range and is stretched to show the brighter stars in the image. (c) A fainter group of stars are clustered within $0''.5$ of Sgr A*. A high pass filter has been used, for display purposes only, to eliminate the seeing halos of the neighboring IRS 16 stars. (d) The correlation of the shift-and-add image, shown in (b), and the diffraction-limited core of the point spread function, scaled to show the stars that are marked as definite detections. The location of stars are easily identified in this crowded field. All images are oriented such that North is up and East is to the left.

Fig. 2.— (a) The point spread function for the 1995 June shift-and-add image as measured from the radial profile of IRS 16 NE. The diffraction limited core, which contains $\sim 10\%$ of the flux, is built up from the brightest speckle in each contributed frame, while the seeing halo results from the fainter surrounding speckles. Airy rings encircle each core indicating that the diffraction-limit has truly been achieved (b) A gaussian fit to the seeing halo has been subtracted from the data (dotted line) to emphasize the Airy ring contribution and the theoretical point spread function of Keck (solid line) is plotted for comparison.

Fig. 3.— The measured positions of stars a 1 arcsec^2 centered on the position of Sgr A* (starred point, which depicts the location of this radio source). Significant velocities, which reach 1400 ± 100 km/sec, are easily detected in this region. Each year’s measurement is represented by a different symbol: 1995 by triangles, 1996 by squares, and 1997 by circles.

Fig. 4.— The positions of the 90 stars that were unambiguously detected in all three years are displayed with point sizes scaled to the stars’ velocities. Proper motion measurements with SNR of at least 4 are plotted as filled points. A clear increase in the velocities is visible at the field center, where stars reach velocities of 1,400 km/sec.

Fig. 5.— The projected stellar velocity dispersion as a function of projected distance from Sgr A* is consistent with Keplerian motion, which implies the gravitational field is dominated by mass within 0.1 pc.

Fig. 6.— The minimum enclosed mass as a function of projected radius inferred from the 30 stars with $v/\sigma_v \geq 4$. The solid curve in the lower right corner is an extrapolation of the enclosed luminous matter curve from Genzel et al. (1996). Each star suggests the presence of a central dark mass of roughly a million M_{\odot} .

Fig. 7.— The enclosed mass as a function of projected distance from Sgr A* are shown for the results of this study (7 filled circles), EG’s proper motion study (4 unfilled circles), Genzel et al. (1996) radial velocity study (13 unfilled squares), and Guesten et al. (1987) measurement of the rotating gas disk (2 unfilled triangles). From 0.1 to 0.015 pc the enclosed mass appears to be constant with a value of $2.6 \times 10^6 M_\odot$. Mathematically, power law dark clusters with $\alpha \geq 3$ fit the observed distributions, however they are not physically tenable (see text). The high density of the central dark mass, which exceeds $10^{12} M_\odot / pc^3$, is indicative of a single supermassive black hole.

Table 1. Keck Proper Motions Measurements

Star ID ^a	Other	K ^{b,c} (mag)	R ^b (arcsec)	ΔRA ^b (arcsec)	ΔDEC ^b (arcsec)	V_{ra} (km/sec)	V_{dec} (km/sec)	Notes
S0-1	S1	14.9	0.114	-0.107	0.039	470 ± 130	-1330 ± 140	1
S0-2	S2	14.1	0.151	0.007	0.151	-290 ± 110	-500 ± 50	1
S0-3	S4	14.7	0.218	0.198	0.090	495 ± 60	300 ± 50	1
S0-4	S8	14.5	0.338	0.300	-0.154	720 ± 80	-530 ± 110	1
S0-5	S9	15.1	0.350	0.212	-0.279	120 ± 140	-630 ± 250	1
S0-6	S10	14.2	0.440	0.148	-0.414	-400 ± 100	230 ± 100	1
S0-7	S6	14.9	0.460	0.453	0.077	480 ± 170	120 ± 130	1
S0-8	-	16.1	0.468	-0.279	0.376	260 ± 260	-850 ± 260	3
S0-9	S11	14.1	0.553	0.150	-0.532	200 ± 60	-80 ± 140	1
S0-10	-	15.2	0.578	0.300	-0.494	120 ± 80	-50 ± 160	3
S0-11	S7	15.5	0.598	0.597	-0.023	-130 ± 70	-220 ± 130	1
S0-12	W6	14.4	0.625	-0.521	0.345	-100 ± 80	210 ± 30	1
S0-13	-	13.5	0.752	0.586	-0.471	-90 ± 60	250 ± 50	3
S0-14	W9	13.8	0.794	-0.740	-0.287	20 ± 90	50 ± 90	1
S0-15	W5	13.8	0.911	-0.852	0.321	-310 ± 60	-310 ± 130	1
S1-1	-	13.3	1.006	1.006	0.018	200 ± 90	60 ± 90	3
S1-2	-	14.9	1.014	-0.055	-1.013	510 ± 110	90 ± 170	3
S1-3	-	12.3	1.016	0.566	0.844	-480 ± 50	150 ± 70	2
S1-4	-	12.9	1.045	0.772	-0.705	410 ± 80	50 ± 100	3
S1-5	-	12.8	1.053	0.433	-0.960	-300 ± 70	230 ± 80	3
S1-6	-	16.0	1.061	-0.822	0.672	-600 ± 210	190 ± 270	3
S1-7	-	16.9	1.063	-0.943	-0.491	-110 ± 250	-200 ± 180	3
S1-8	W11	14.2	1.077	-0.659	-0.852	160 ± 60	-240 ± 90	1
S1-9	16 NW	10.1	1.190	0.027	1.190	310 ± 60	380 ± 110	2
S1-10	W8	15.0	1.204	-1.199	-0.114	120 ± 170	330 ± 60	1
S1-11	16 C	10.0	1.294	1.218	0.436	-370 ± 60	380 ± 40	2
S1-12	W13	13.7	1.316	-0.852	-1.003	220 ± 70	20 ± 60	1
S1-13	W12	14.2	1.357	-1.032	-0.880	-410 ± 120	-260 ± 140	1
S1-14	W10	12.9	1.371	-1.340	-0.287	-20 ± 70	-100 ± 60	1
S1-15	W4	14.3	1.410	-1.311	0.519	30 ± 160	-30 ± 90	1
S1-16	16 SW	10.2	1.442	1.055	-0.983	170 ± 60	150 ± 40	2
S1-17	-	12.4	1.549	0.545	-1.450	-200 ± 50	-80 ± 50	3
S1-18	-	15.4	1.599	-0.638	1.466	-220 ± 190	90 ± 120	3
S1-19	-	13.8	1.630	0.382	-1.584	20 ± 50	-60 ± 120	3
S1-20	-	12.7	1.641	0.414	1.588	240 ± 80	160 ± 50	2
S1-21	W7	13.7	1.653	-1.648	0.137	160 ± 120	-200 ± 60	1
S1-22	W14	12.8	1.704	-1.628	-0.503	70 ± 60	-5 ± 80	1
S1-23	-	11.9	1.718	-0.900	-1.463	-20 ± 80	10 ± 90	2
S1-24	-	11.6	1.729	0.759	-1.554	-160 ± 40	-210 ± 70	2
S1-25	-	13.8	1.810	1.688	-0.655	-70 ± 90	240 ± 50	3

Table 1—Continued

Star ID ^a	Other	K ^{b,c} (mag)	R ^b (arcsec)	ΔRA ^b (arcsec)	ΔDEC ^b (arcsec)	V_{ra} (km/sec)	V_{dec} (km/sec)	Notes
S2-1	29 S, W1	11.4	2.024	-1.801	0.925	-40 ± 50	50 ± 50	1
S2-2	-	14.2	2.068	-0.536	1.998	140 ± 140	200 ± 40	3
S2-3	-	14.5	2.081	-1.513	-1.430	110 ± 110	260 ± 230	3
S2-4	-	12.1	2.085	1.457	-1.491	140 ± 70	230 ± 40	3
S2-5	-	13.3	2.090	1.905	-0.859	240 ± 110	80 ± 80	3
S2-6	-	11.9	2.097	1.598	-1.358	200 ± 60	230 ± 50	3
S2-7	-	13.6	2.099	1.056	1.814	-60 ± 90	220 ± 80	3
S2-8	W2	12.3	2.108	-1.940	0.824	150 ± 110	120 ± 90	1
S2-9	16 CC	10.6	2.117	2.055	0.508	-120 ± 50	170 ± 60	2
S2-10	29 N	9.9	2.125	-1.587	1.413	200 ± 100	-140 ± 100	2
S2-11	-	11.9	2.128	2.034	-0.625	-130 ± 80	110 ± 70	2
S2-12	-	15.8	2.129	1.759	1.200	-220 ± 70	-340 ± 170	3
S2-13	-	11.3	2.164	-0.015	-2.164	-90 ± 140	-100 ± 90	2
S2-14	-	15.5	2.170	-1.501	-1.567	180 ± 350	340 ± 270	3
S2-15	16 SE1	10.8	2.195	1.861	-1.164	170 ± 60	240 ± 40	2
S2-16	-	11.8	2.232	-0.911	2.038	-200 ± 90	10 ± 40	2
S2-17	-	10.9	2.259	1.270	-1.868	260 ± 60	180 ± 40	2
S2-18	-	13.2	2.317	-0.901	-2.135	-320 ± 230	140 ± 140	2
S2-19	-	12.6	2.334	0.527	2.273	-180 ± 180	90 ± 40	3
S2-20	-	16.4	2.349	1.711	1.609	50 ± 200	340 ± 360	3
S2-21	-	13.6	2.363	-1.696	-1.645	420 ± 110	80 ± 100	1
S2-22	-	13.0	2.389	2.371	-0.287	-140 ± 60	330 ± 40	1
S2-23	-	14.9	2.460	1.700	1.779	240 ± 130	-100 ± 170	3
S2-24	W16	13.9	2.464	-2.281	-0.934	-140 ± 220	110 ± 230	1
S2-25	-	14.1	2.587	0.790	-2.463	-200 ± 290	200 ± 200	3
S2-26	-	13.5	2.603	0.732	2.497	340 ± 120	-420 ± 100	3
S2-27	-	13.0	2.755	0.269	2.742	-170 ± 270	-690 ± 190	3
S2-28	-	14.5	2.847	2.697	-0.913	-170 ± 110	250 ± 170	3
S2-29	-	15.4	2.912	2.004	-2.113	-240 ± 310	40 ± 350	3
S2-30	-	15.3	2.913	2.913	-0.042	220 ± 200	30 ± 240	3
S2-31	-	13.0	2.918	2.911	-0.195	-360 ± 60	140 ± 50	3
S2-32	-	12.1	2.981	1.148	2.751	120 ± 210	260 ± 110	2
S3-1	16 NE	9.0	3.094	2.892	1.100	160 ± 90	-290 ± 30	2
S3-2	-	12.1	3.116	3.066	0.558	210 ± 90	80 ± 70	3
S3-3	-	15.0	3.177	3.100	-0.695	110 ± 300	190 ± 470	3
S3-4	-	14.4	3.203	3.157	-0.543	50 ± 140	240 ± 150	3
S3-5	16 SE2	12.0	3.205	2.974	-1.196	50 ± 90	260 ± 130	2
S3-6	-	12.8	3.260	3.259	0.080	90 ± 100	-280 ± 70	3
S3-7	-	14.1	3.283	2.014	-2.592	-90 ± 260	200 ± 240	3
S3-8	-	14.3	3.495	3.463	-0.471	-90 ± 180	10 ± 170	3

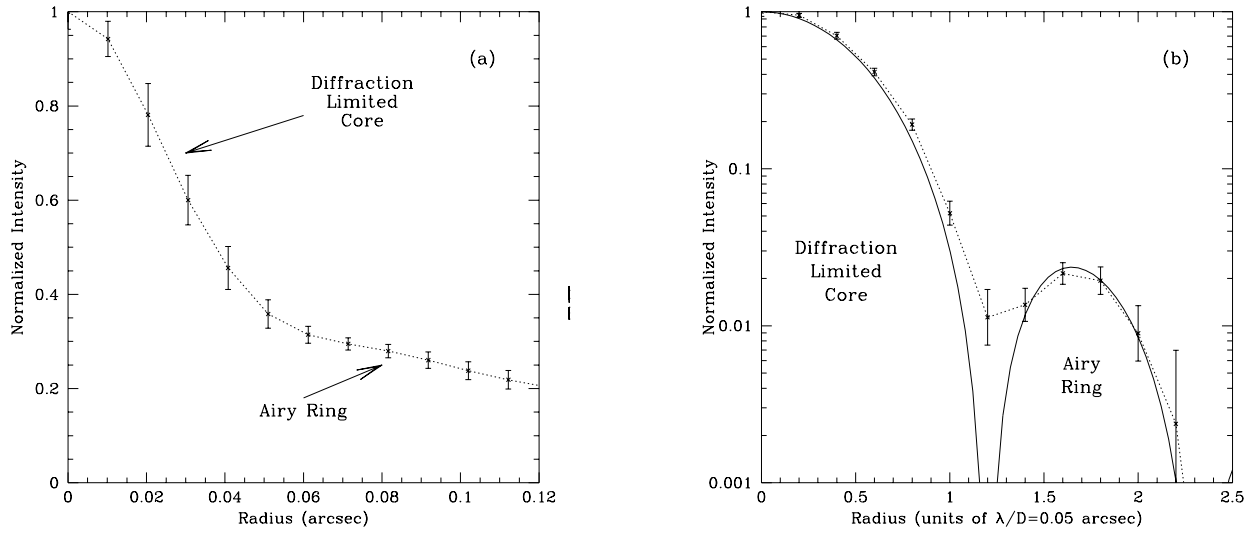


Figure 2

Table 1—Continued

Star ID ^a	Other	K ^{b,c} (mag)	R ^b (arcsec)	ΔRA ^b (arcsec)	ΔDEC ^b (arcsec)	V_{ra} (km/sec)	V_{dec} (km/sec)	Notes
S3-9	-	12.4	3.510	3.300	-1.195	-80 ± 70	20 ± 60	3
S3-10	-	12.0	3.586	3.395	-1.156	-60 ± 70	-10 ± 120	3
S3-11	-	14.8	3.590	3.034	-1.919	-120 ± 200	240 ± 130	3
S3-12	21	11.8	3.695	2.484	-2.736	-270 ± 170	170 ± 110	2
S3-13	-	13.6	3.939	3.840	0.875	210 ± 100	0 ± 310	3
S4-1	-	13.7	4.130	4.116	-0.331	0 ± 210	-320 ± 130	3
S4-2	-	12.7	4.144	3.779	1.702	-160 ± 100	-360 ± 80	3
S4-3	-	13.5	4.210	4.208	0.131	340 ± 280	-140 ± 100	3
S4-4	-	12.1	4.320	3.647	-2.317	-100 ± 130	-110 ± 170	3
S4-5	-	12.0	4.339	3.710	-2.249	-160 ± 100	-150 ± 130	3

^a The naming convention adopted is designed to directly convey relevant information about the location of the source relative to the position of SgrA*. Adopting the SgrA* position given by Menton et al. (1997), which is accurate to 0.03 arcseconds, we divide the surrounding field into concentric arcsecond-wide annuli centered on SgrA*. Stars lying in the central circle, which has radius 1 arcsecond, are given the names S0-1, S0-2, S0-3, etc. Stars lying in the annulus between radii of 1 to 2 arcseconds are given the names S1-1, S1-2, and so on. The number immediately following "S" thus refers to the inner radius of the annulus in which the star lies. The number following the hyphen is ordered in the sense of increasing distance from SgrA* within each annulus. Of course there are more stars in each annulus than in our proper motion sample listed here. When this nomenclature is applied to future lists of new stars, the number following the hyphen will continue to be incremented within each annulus, ordered within each new list of added stars in the sense of increasing distance from SgrA*

^bThe epoch of the brightness and positional measurement is 1995.4.

^cThe brightness of each star is assessed by carrying out aperture photometry on the "cores" with an the object radius extending from 0 to 0''.06, a sky annulus ranging from 0''.06 to 0''.09, and a zero point determined by IRS 16 NE which is assumed to have a K magnitude of 9.0.

Note. — 1 - additional measurements of these stars can be found in Genzel et al. (1997); 2 - additional measurements of these stars can be found in Eckart & Genzel (1997); 3 - this is the first measurement of these stars' proper motions

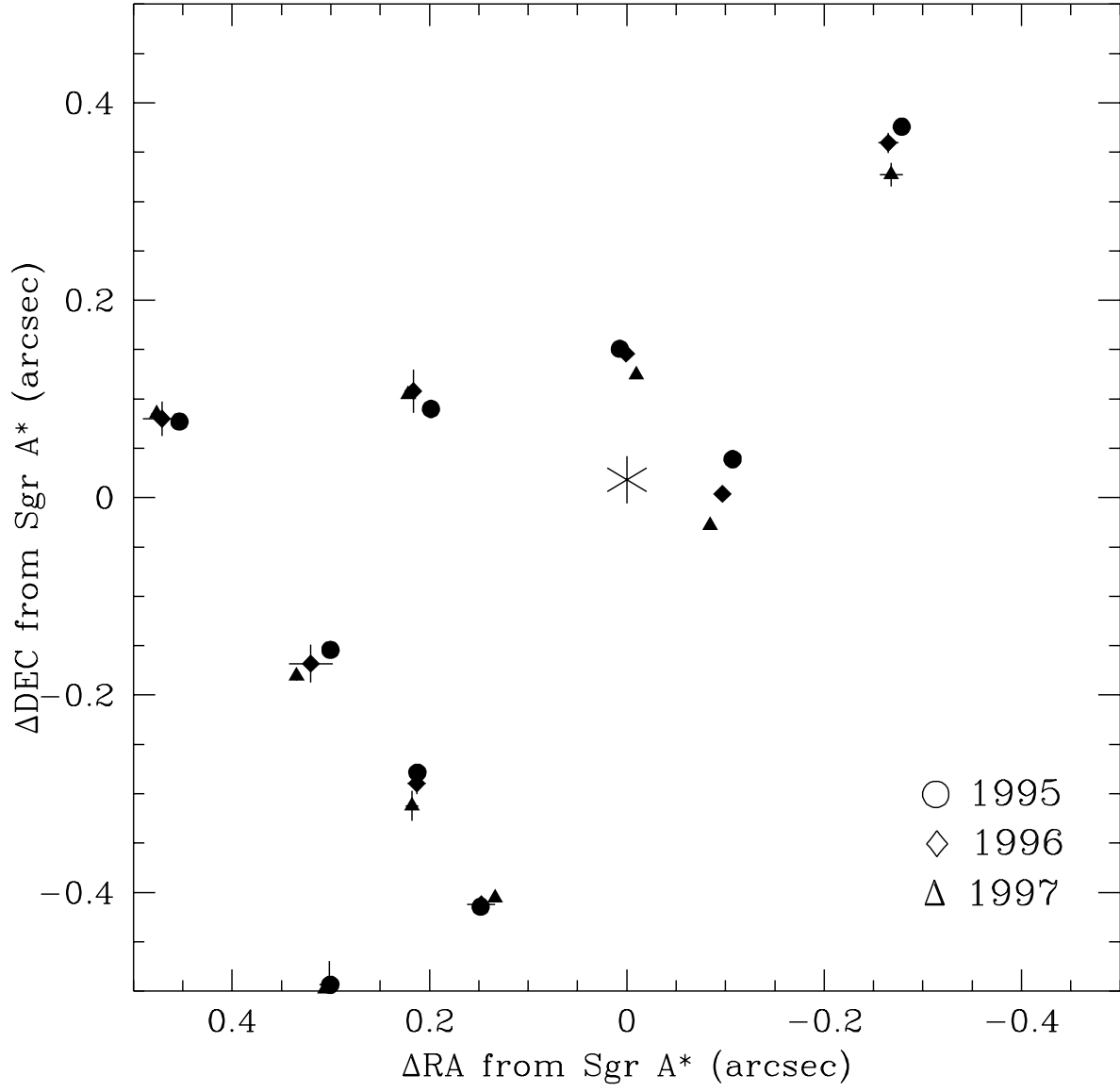


Figure 3

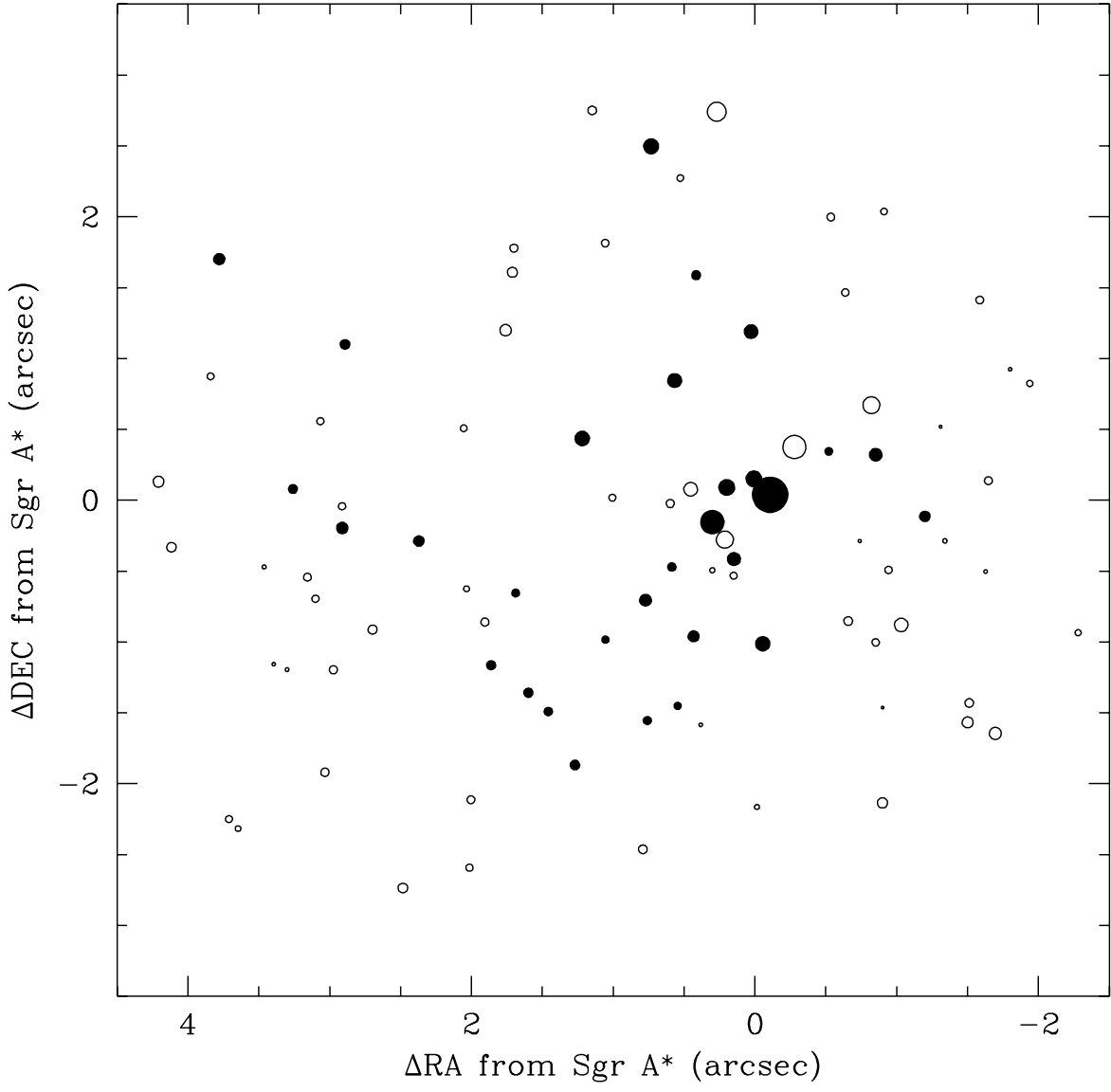


Figure 4

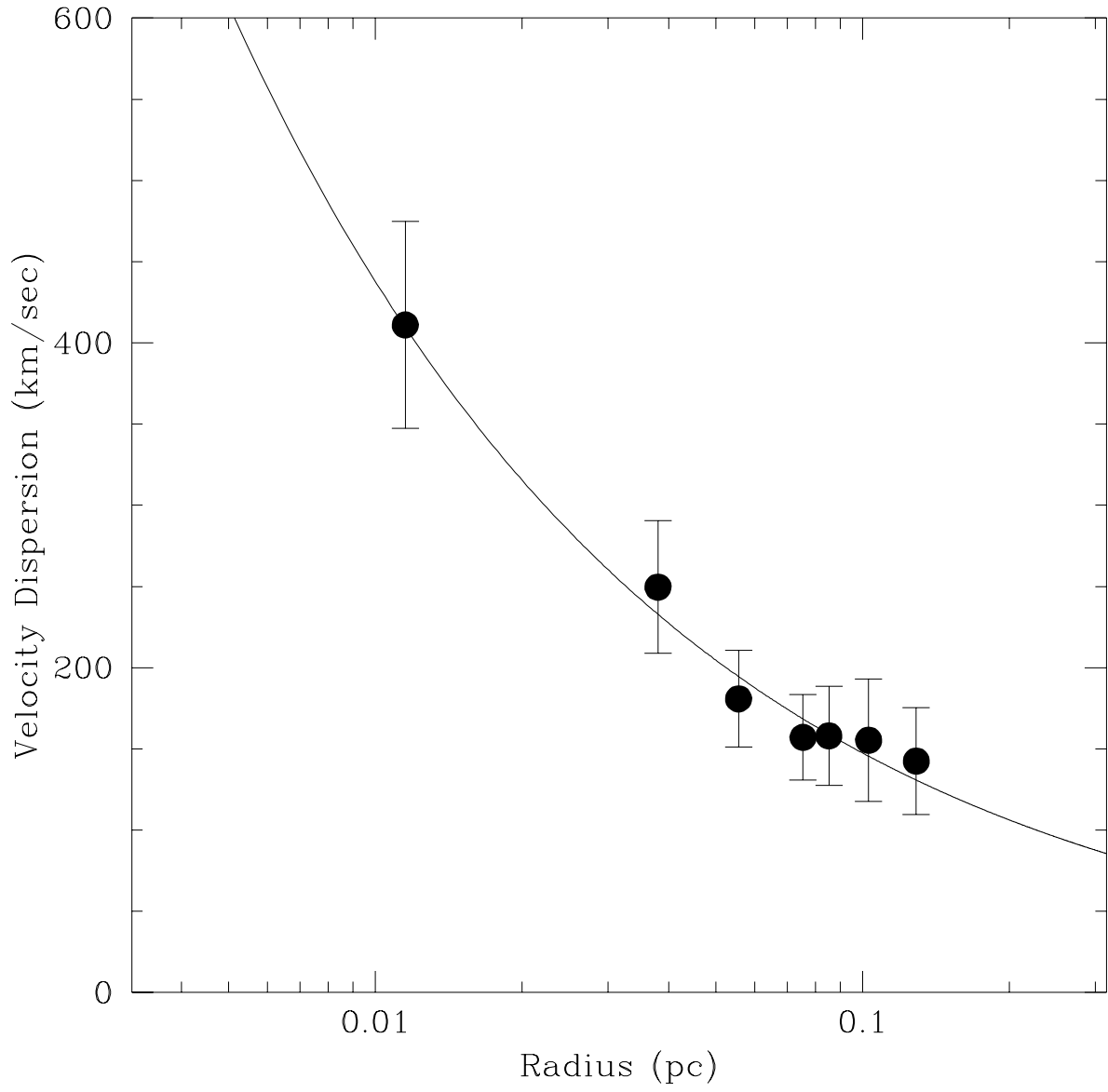


Figure 5

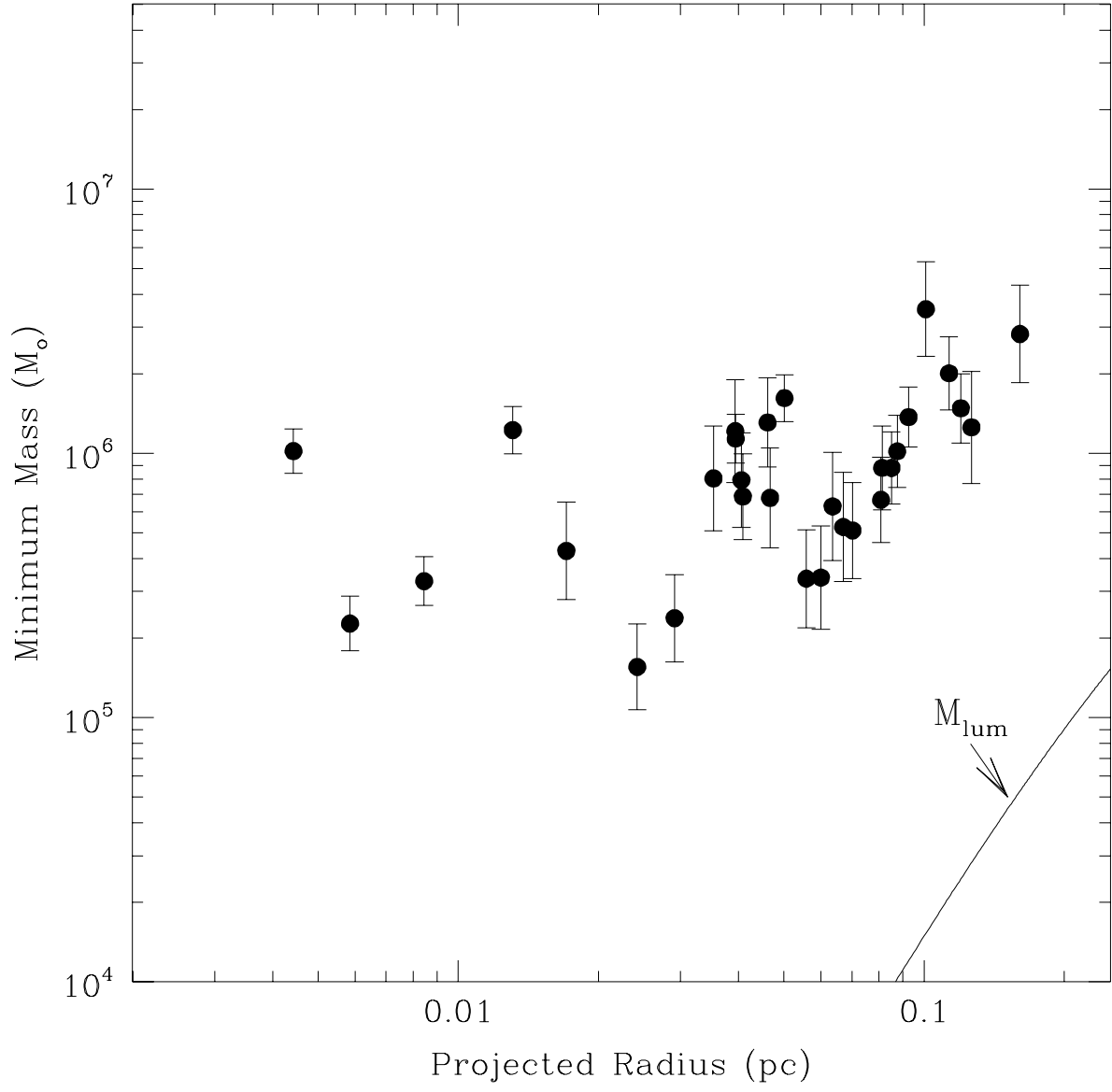


Figure 6

This figure "fig1.jpg" is available in "jpg" format from:

<http://arXiv.org/ps/astro-ph/9807210v2>

This figure "fig7.gif" is available in "gif" format from:

<http://arXiv.org/ps/astro-ph/9807210v2>